

Numerical Investigation of Flow and Combustion in a Single-Element GCH₄/GOX Rocket Combustor: Aspects of Turbulence Modeling

A. Chemnitz*, T. Sattelmayer†, C. Roth‡, O. Haidn§
Technische Universität München, 80333 Munich, Germany

Y. Daimon¶
Japan Aerospace Exploration Agency, 305-8505 Tsukuba, Ibaraki, Japan

R. Keller||, P. Gerlinger**
University of Stuttgart, 70569 Stuttgart, Germany

J. Zips††, M. Pfitzner‡‡
Universität der Bundeswehr München, 85577 Neubiberg, Germany

A comparison of the numerical predictions of several groups modeling the reacting flow inside a GCH₄/GOX single element rocket combustion chamber is conducted. The focus is placed on turbulence quantities and their influence on the computed mean fields. However, subject of this paper is not a pure study of turbulence model variation but it aims at showing their effect within the framework of different overall setups. These comprise differences in combustion models as well as codes used. Several RANS approaches incorporating the Boussinesq approximation for the modeling of Reynolds stresses are considered. Turbulent heat and mass transfer are modeled via turbulent Prandtl and Schmidt numbers. Characteristic tendencies of the turbulence models are observed across the different codes and combustion models. Furthermore, the relevance of turbulence modeling parameters depends on the combustion modeling approach. An influence of the code used is found as well.

Nomenclature

A	area
\mathcal{E}	conserved energy
f	mixture fraction
\bar{f}	global mixture fraction
\mathcal{F}_t	turbulent flux
h_{abs}	absolute enthalpy
h_f^0	heat of formation
h_s	sensible enthalpy

*PhD student, Institute for Thermodynamics, Boltzmannstr. 15, 85748 Garching, Germany

†Full Professor, Institute for Thermodynamics, Boltzmannstr. 15, 85748 Garching, Germany

‡PhD student, Institute for Flight Propulsion, Boltzmannstr. 15, 85748 Garching, Germany

§Full Professor, Institute for Flight Propulsion, Boltzmannstr. 15, 85748 Garching, Germany

¶Researcher, Research and Development Directorate, 2-1-1 Sengen, Tsukuba, Ibaraki, Japan, Member

||PhD student, IVLR, Pfaffenwaldring 38-40, 70569 Stuttgart, Germany

**Full Professor, IVLR, Pfaffenwaldring 38-40, 70569 Stuttgart, Germany

††PhD student, Institute for Thermodynamics, Werner-Heisenberg-Weg 39, 85577 Neubiberg, Germany

‡‡Full Professor, Institute for Thermodynamics, Werner-Heisenberg-Weg 39, 85577 Neubiberg, Germany

k	turbulent kinetic energy
\dot{m}	mass flow
OFR	oxidizer to fuel ratio
Pr_t	turbulent Prandtl number
q	square root of turbulent kinetic energy
Sc_t	turbulent Schmidt number
T	temperature
c_p	isobaric heat capacity
u	velocity
x	axial coordinate
y^+	dimensionless wall distance
\mathcal{Y}	atomic mass fraction

Subscripts

f	fuel
ox	oxidizer
Pr	Prandtl normalized
s	shape
Sc	Schmidt normalized

Symbols

$\Delta\dot{Q}$	integral upstream heat release rate
ϵ	turbulent dissipation
η_f	mixedness
η_h	enthalpy stratification
μ_t	turbulent viscosity
ρ	mean density
ϕ	generic quantity
ω	specific turbulent dissipation

Superscripts

$-$	axial average, mass flow average
\sim	Favre average
$'$	turbulent fluctuation

Acronyms

BW	Institute for Thermodynamics, Universität der Bundeswehr München.
GCH ₄	Gaseous Methane.
GOX	Gaseous Oxygen.
IVLR	IVLR, University of Stuttgart.
JAXA	Japan Aerospace Exploration Agency.
LFA	Institute for Flight Propulsion, Technische Universität München.
TCI	Turbulence-Chemistry Interaction.
TD	Institute for Thermodynamics, Technische Universität München.

I. Introduction

The numerical simulation of internal flows using Computational Fluid Dynamics is of high relevance in contemporary design processes of rocket combustion chambers. With growing interest in methane as possible fuel substitute for hydrogen, the need for accurate flow field predictions in corresponding configurations increases. During the Combustion Modeling Workshop in the frame of the SFB/TRR 40 Summer Program 2015 different approaches have been taken to model the flow inside a single element combustion chamber operated with Gaseous Oxygen (GOX)/Gaseous Methane (GCH₄). A comparison of the first results showed significant differences.¹ The predicted wall heat fluxes as well as the wall pressure distributions varied over a notable range across the different simulations. In the flow fields, these tendencies were reflected in differing flame lengths and temperature distributions. As work on this test case is continued, in the present paper a more detailed analysis of the underlying effects is carried out. This shall generate a better understanding of the influencing factors and thus potentially increase the accuracy of simulations in the future.

There are multiple, coupled aspects that are relevant for the form of the final flow fields. However, a comprehensive analysis would go beyond the scope of a single paper. Thus, this publication focuses on the influence of turbulence modeling. A comparison of full three-dimensional computations to experimental data is conducted in Ref. 2. Aspects of chemistry modeling together with Turbulence-Chemistry Interaction (TCI) are covered in Ref. 3.

The data accessed in the experiment, i.e. wall heat flux and wall pressure distribution, are not only of practical relevance but also provide the basis for simulation validation. Thus, the influence on these quantities is of special interest when studying the effect of turbulence. However, the validation quantities depend on various flow effects. The general structure taken as basis in this paper is illustrated in figure 1. The validation quantities are determined by certain mean flow effects like heat release or enthalpy distribution. These are influenced by turbulence, which is accounted for in the flow equations via the turbulent viscosity. This again is obtained from turbulence quantities, which are provided by the turbulence model employed.

To access the effect of turbulence modeling on the validation quantities, two approaches are used in this paper. First, sensitivity to turbulence modeling parameters, namely the turbulent Prandtl and Schmidt numbers, is studied. This is of particular relevance on the first and second level (cf. figure 1). Second, the effects underlying the validation quantities are traced back to the turbulence modeling. This is done by relating observations made at one evaluation level to those made at the layer below until the level of turbulent quantities is reached.

The aim of this paper is to access the role of turbulence in the context of the different setups used rather than to conduct a strict study of turbulence modeling. To allow for cost effective parameter variations, two-dimensional simulations are employed. Since the chamber under consideration is of quadratic cross section, this means a geometric simplification. Correspondingly, experimental results are included only to allow an

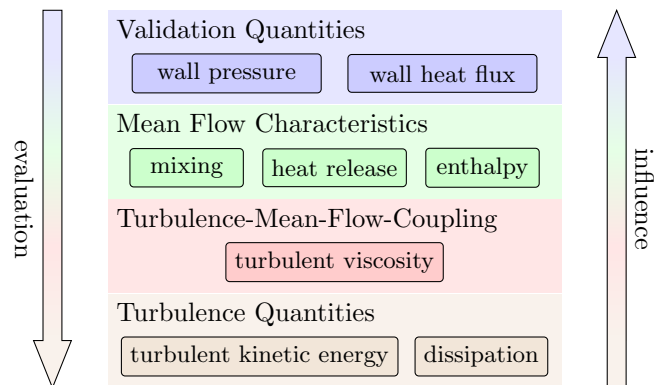


Figure 1. Evaluation levels

assessment of the tendencies observed rather than for exact validation. The approaches under consideration comprise the following variations:

- Chemistry modeling – finite rate / flamelet
- TCI – PDF-Integration / laminar chemistry
- Turbulence models – $k-\omega$ -sst / $k-\epsilon$ / $q-\omega$

The paper is structured as follows: First, the test case providing the experimental background for the simulations is introduced, followed by a description of the numerical setups. Then, quantities used for the evaluation are defined before discussing the results. Finally, a conclusion is given.

II. Test Case

The test case under consideration is defined in Ref. 4. At this point only a brief summary outlining the experimental setup is given. GCH_4 and GOX are injected coaxially into the combustor through a single injector located at the chamber axis. The chamber has a rectangular cross section of 12 mm x 12 mm and is approximately 300 mm long. It ends in a two-dimensional nozzle with a contraction ratio of 2.5. The operating conditions are summarized in table 1. Data provided from the experiment are axially resolved wall pressure, wall temperature and the reconstructed wall heat flux.

Table 1. Operating conditions

operating pressure	OFR	\dot{m}_{ox}	\dot{m}_f	\dot{m}_{tot}
~ 19 bar	2.62 $\frac{kg}{s}$	0.045 $\frac{kg}{s}$	0.017 $\frac{kg}{s}$	0.062 $\frac{kg}{s}$

III. Numerical Setup

Altogether, this paper is based on results of five different groups computed with four codes and various turbulence models. In this section the underlying setups are specified. This comprises the group specific simulation approaches as well as the computational domain and boundary conditions.

A. General Setup

All simulations solve the Navier-Stokes equations with the ideal gas equation of state. Two different combustion modeling approaches are used. The finite rate setups solve transport equations for all species, while the flamelet approaches base on mixture fraction (in the following these will be referred to as mixture fraction based approaches synonymously). A combustion mechanism developed at DLR,⁵ comprising 21 species in 97 reactions is used to model chemical kinetics for all setups except for that of BW, where the GRI-3.0⁶ mechanism is used. For every setup, turbulent Prandtl and Schmidt numbers (cf. section IV A) are set to 0.7, 0.9 and 1.1 each. The specifications of the different groups' approaches are given in the following and are summarized in table 2.

1. Institute for Thermodynamics, Technische Universität München (TD)

The simulations of TD are performed with the commercial solver ANSYS Fluent.⁷ Combustion is modeled using a semi-diabatic flamelet approach: While the local enthalpy is used for the calculation of temperature, the local flow composition is calculated from adiabatic conditions. That is to say, the local enthalpy does not affect the chemical reactions. Non-equilibrium effects are incorporated via scalar dissipation and TCI is modeled assuming a β -PDF for the mixture fraction. For energy conservation the total enthalpy is used.

Turbulence closure is obtained with the $k-\epsilon$ model.⁸ Wall near turbulence is modeled using Fluent's enhanced wall treatment. This corresponds to a two-layer- $k-\epsilon$ model at resolved boundary layers ($y^+ < 1$) as they are present at the chamber wall.

Table 2. Setup overview

	TD	LFA	JAXA	IVLR	BW
Solver	Fluent	Fluent	CRUNCH CFD	TASCOM3D	OpenFOAM
Combustion Model	Flamelet	Flamelet	Finite Rate	Finite Rate	Flamelet
TCI	β -pdf	β -pdf	laminar	laminar	β -pdf
Turbulence Model	k- ϵ	k- ω -sst	k- ϵ k- ω -sst	q- ω k- ω -sst	k- ω -sst

2. Institute for Flight Propulsion, Technische Universität München (LFA)

The LFA results are computed with ANSYS Fluent⁹ using a comparable setup as TD. However, for turbulence modeling the k- ω -sst model¹⁰ is used. This is done to achieve coverage of a broader range of turbulence models for this solver.

3. Japan Aerospace Exploration Agency (JAXA)

The JAXA results are obtained using the density based solver CRUNCH CFD. Combustion is modeled with a laminar finite rate approach. For turbulence closure, the k- ϵ and the k- ω -sst model are used.

4. IVLR, University of Stuttgart (IVLR)

IVLR uses the in-house CFD solver TASCOM3D (Turbulent All-Speed Combustion Multigrid). The solver is density based using high order spatial discretization (5th order MLP^{1d}). Chemical reactions are accounted for via finite rate chemistry without TCI. For energy conservation the total energy is employed. Two different turbulence models are used in this paper: The k- ω -sst model by Menter and the q- ω -model by Coakley.¹¹

5. Institute for Thermodynamics, Universität der Bundeswehr München (BW)

BW uses a solver based on OpenFOAM^a. OpenFOAM is a fully parallelized open-source CFD software that has been extended by BW to allow for simulations using a semi-diabatic flamelet tabulation as described above. The species composition is obtained via a flamelet approach with a β -PDF for the mixture fraction. Thermodynamically consistent, the temperature is then calculated from the transported total enthalpy and the respective flow composition using NASA polynomials. Turbulence closure is obtained via the k- ω -sst model¹⁰ without wall functions and using default coefficients. OpenFOAM is a widely used platform and has been applied to simulate a multitude of physical processes. Recently, the framework has been used to study both non-reacting^{12,13} and reacting¹⁴ flows at rocket-like conditions.

B. Computational Domain

As simulations are performed in 2D, the rectangular geometry has to be approximated. Thereto an axis-symmetric setup is considered. Radii of chamber and nozzle throat are chosen to preserve the respective cross-sectional area. The nozzle is taken as conical with the axial dimensions remaining unchanged. At the inlet section, the injection pipes are resolved up to the manifolds. The computational geometry is shown in figure 2. To allow the different groups to adapt to their specific solver requirements, each is using its own computational grid. The key parameters are given in table 3.

C. Boundary Conditions

The inflow boundary conditions are block profiles, based on the mass flows stated in table 1. Experimental temperatures of fuel and oxidizer are provided in Ref. 4. Turbulent kinetic energy is calculated with a turbulent intensity of 5 %. Turbulent dissipation quantities are obtained from the respective correlations of developed pipe flow. The wall temperature along the chamber is set to the experimentally determined

^awww.openfoam.com

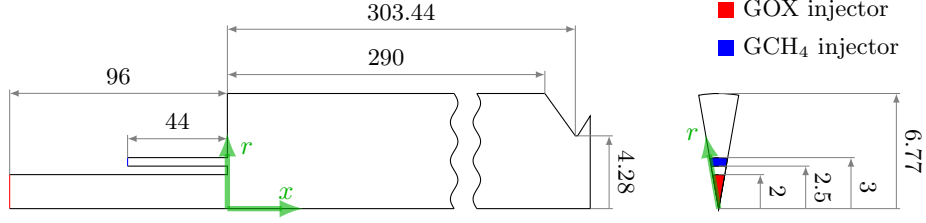


Figure 2. Domain geometry with main dimensions (in mm)

Table 3. Mesh parameters

	No. of cells	Wall resolution / mm	Post tip resolution / cells
TD	$128 \cdot 10^3$	$5 \cdot 10^{-4}$	24
LFA	$82 \cdot 10^3$	$5 \cdot 10^{-4}$	38
JAXA	$58 \cdot 10^3$	$1 \cdot 10^{-3}$	40
IVLR	$43 \cdot 10^3$	$1 \cdot 10^{-3}$	32
BW	$89 \cdot 10^3$	$1 \cdot 10^{-3}$	5

temperature profile (cf. Ref. 4).

IV. Evaluation Criteria

To evaluate the simulation results at the different levels introduced in section I, several quantities are used. In the following an overview of the most important ones and their respective relevance is given. In general, three categories can be identified: pure turbulence quantities, coupling parameters closing the gap between turbulence model and mean flow and finally global mean flow quantities.

A. Turbulence Quantities and Turbulence-Mean-Flow-Coupling

The most immediate influence of turbulence on the mean flow fields is represented by the turbulent viscosity μ_t . It directly influences the turbulent transport of momentum, species and energy. The turbulent stresses in the momentum equation are modeled as

$$\widetilde{u'_i u'_j} = -\frac{\mu_t}{\rho} \left(\frac{\partial u_i}{\partial x_j} + \frac{\partial u_j}{\partial x_i} - \frac{2}{3} \frac{\partial u_k}{\partial x_k} \delta_{ij} \right) + \frac{2}{3} k \delta_{ij} \quad . \quad (1)$$

Here u is the mean velocity, u' denotes the turbulent velocity fluctuation, $\widetilde{\cdot}$ is the Favre average, ρ the density and k the turbulent kinetic energy (see below). The specific transport equations solved for flow composition and energy vary with the setup considered. However, in any case the turbulent flux of the conserved energy \mathcal{E} is computed according to:

$$\mathcal{F}_{t,e,i} = \frac{\mu_t}{Pr_t} \frac{\partial \mathcal{E}}{\partial x_i} \quad . \quad (2)$$

Analogously for turbulent transport of species or mixture fraction the flux is modeled via

$$\mathcal{F}_{t,y/f,i} = \frac{\mu_t}{Sc_t} \frac{\partial \phi}{\partial x_i} \quad (3)$$

where ϕ represents the species mass fractions or the mixture fraction respectively.

A commonality between the turbulence models considered is the use of two-equation-models to obtain the field of turbulent viscosity. For this type of models, that quantity is calculated from a turbulent length

and time scale. All setups in this study transport the turbulent kinetic energy k or its square root q . It is defined as

$$k = q^2 = \frac{1}{2} \widetilde{u'_i u'_i} \quad . \quad (4)$$

The second transported quantity is either the turbulent dissipation ϵ or the specific turbulent dissipation ω . For the turbulent viscosity the following approximately holds:

$$\mu_t \sim \frac{k^2}{\epsilon} \text{ and } \mu_t \sim \frac{k}{\omega} \quad . \quad (5)$$

For the q - ω model, an additional factor of 0.09 is included in the calculation of the turbulent viscosity, which is not present in the k - ω -sst model. This has to be considered when comparing the respective fields.

B. Derived Mean Flow Parameters

As outlined before, several mean flow quantities are of relevance for understanding the validation data. A key parameter for the axial development of pressure and wall heat flux is the heat release prediction. This quantity is closely related to the mixing process, for which turbulent transport plays a dominating role. This is particularly true for the region reasonably far downstream of the face plate. Besides species mixing, the radial distribution of energy in the chamber is another parameter that characterizes the resulting flow field.

First, the one-dimensional axial development of the heat release is considered. Since the simulations are of steady state type, this can be done via the local enthalpy of formation flow. The amount of chemical power released up to axial position x can be calculated as

$$\Delta \dot{Q}(x) = \dot{m}_f h_{f,f}^0 + \dot{m}_{ox} h_{f,ox}^0 - \int_{A(x)} \rho u_x h_f^0 dA \quad . \quad (6)$$

Here \dot{m}_f and \dot{m}_{ox} are the inlet mass flows of fuel and oxidizer respectively, h_f^0 is the heat of formation and A the local crosssectional area. Thus, the heat released, $\Delta \dot{Q}$, corresponds to the axial integral of the upstream heat release rate.

To study the axial evolution of the mixing process, a mixedness parameter η_f is defined. It quantifies the radial stratification of mixture fraction f at an axial position x :

$$\eta_f(x) = 1 - \left[\frac{\int_{A(x)} (f - \bar{f})^2 \rho u_x dA}{\dot{m}_f \cdot (f_f - \bar{f})^2 + \dot{m}_{ox} \cdot (f_{ox} - \bar{f})^2} \right]^{0.5} \quad (7)$$

where \bar{f} denotes the global mixture fraction at perfect mixing of fuel and oxidizer streams. The mixedness parameter varies between 0 at complete separation of fuel and oxidizer and 1 at perfect mixedness. To allow a consistent comparison of all approaches, the mixture fraction is taken as the local mass fraction originating from fuel:

$$f = 1 - \mathcal{Y}_O \quad (8)$$

where \mathcal{Y}_O is the local atomic mass fraction of oxygen, calculated from all species.

To capture the enthalpy distribution across the chamber, an enthalpy stratification parameter is used, which is based on the sensible enthalpy

$$h_s = \int_{T_{ref}}^T c_p dT \quad (9)$$

where c_p denotes the isobaric heat capacity and T the temperature. As reference value the mass flow averaged sensible enthalpy at the respective axial position, $\bar{h}_s(x)$, is taken. The stratification parameter is then defined by normalizing the mass flow weighted mean of deviation between local sensible enthalpy and this reference value:

$$\eta_h(x) = \frac{\int_{A(x)} \rho u_x |h_s - \bar{h}_s| dA}{\bar{h}_s(x) \int_{A(x)} \rho u_x dA} \quad . \quad (10)$$

Finally, Prandtl or Schmidt normalized values of a quantity ϕ are defined as

$$\phi_{Sc/Pr} = \frac{\phi}{\phi|_{Sc=0.7/Pr=0.7}} \quad (11)$$

This allows to study the influence of a variation of turbulent Prandtl or Schmidt number alone while keeping the value of the other parameter constant.

Summing up, the turbulent kinetic energy k together with a turbulent dissipation quantity characterizes turbulence. Its local influence on the mean flow is represented via turbulent viscosity. On the mean flow level the quantity $\Delta\dot{Q}$ is a measure for heat release, η_f describes mixing and η_h enthalpy stratification.

V. Results

In this section the results obtained with the setups described above are studied. The discussion is structured following the level approach introduced in section I (cf. figure 1) from top to bottom.

A. Validation Quantities

The first level to be studied comprises the validation data provided for the test case. Since the quantities on this level do not explicitly describe turbulence, the focus is placed upon the effects of the turbulent Prandtl and Schmidt numbers.

The computed wall pressure distributions are shown in figure 3 together with the experimental data. The colored areas depict the range spanned by the different turbulent Prandtl numbers. All results are sensitive to both turbulent Prandtl and Schmidt number. For most of the cases the lowest turbulent Schmidt number of $Sc_t = 0.7$ matches the pressure level of the experiment closest. The predictions of IVLR, TD and JAXA lie within the same range, while the setups combining a k- ω -sst model with a flamelet approach (LFA and BW) are considerably lower. With an increase of the turbulent Schmidt number the pressure level of all simulations decreases. At the same time the spreading between the different setups increases. However, the results of IVLR-sst and IVLR-q- ω remain close to each other.

To further quantify the influence of the turbulent Schmidt and Prandtl number, the pressure change is studied. For all cases the axial variation of the Prandtl or Schmidt normalized wall pressure distribution (cf. Eq. (11)) is low compared to its axial mean value, i.e. $|p_{Sc/Pr} / \bar{p}_{Sc/Pr} - 1| < 1\%$. Accordingly, the relative wall pressure change can be approximated by its axial mean and reduces to a single value per case.

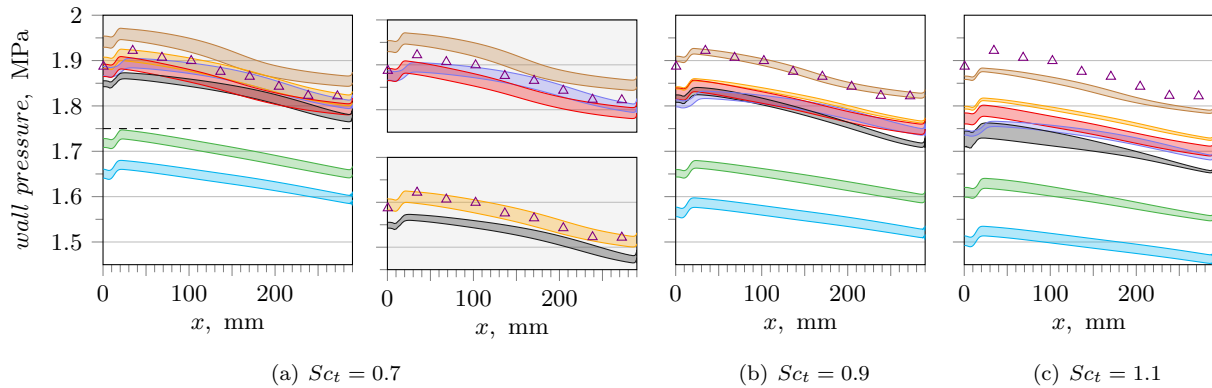


Figure 3. Wall pressure distribution; the colored area corresponds to the range spanned by the different turbulent Prandtl numbers; — TD k- ϵ , — LFA k- ω -sst, — JAXA k- ϵ , — JAXA k- ω -sst, — IVLR q- ω , — IVLR k- ω -sst, — BW k- ω -sst, Δ experimental data

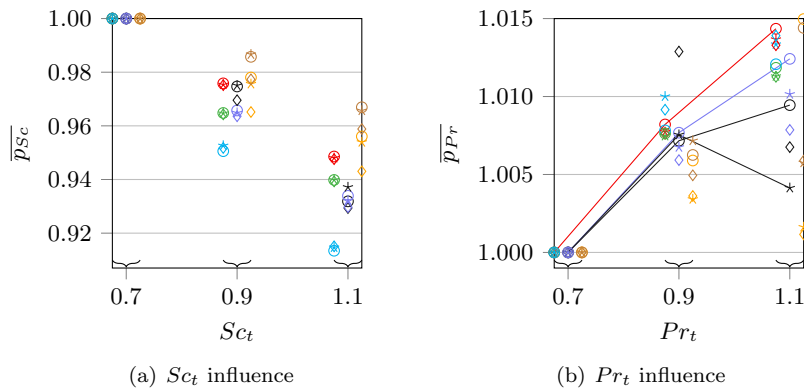


Figure 4. Relative pressure change; lines included for the visualization of tendencies; — TD k- ϵ , — LFA k- ω -sst, — JAXA k- ϵ , — JAXA k- ω -sst, — IVLR q- ω , — IVLR k- ω -sst, — BW k- ω -sst; $\circ Pr_t / Sc_t = 0.7$, $\star Pr_t / Sc_t = 0.9$, $\diamond Pr_t / Sc_t = 1.1$

The corresponding data are plotted in figure 4. The importance of turbulent Prandtl and Schmidt number clearly differs. The pressure change lies between about 2 % and 7 % for the variation of turbulent Schmidt number, while the influence of turbulent Prandtl number remains below 1.5 %. Furthermore, the indirect effects of the turbulent parameters are different. In this regard there is also a dependence on the combustion model. While the flamelet results do not show any significant effect of the value of turbulent Prandtl number at which a turbulent Schmidt number variation is carried out, the finite rate results, particularly those of JAXA, clearly do (cf. figure 4(a)). In turn, most of the setups show an effect of the turbulent Schmidt number level at which the turbulent Prandtl number is varied (cf. figure 4(b)). Again, the influence on the pressure is stronger for the finite rate results. There the turbulent Schmidt number at which the Prandtl number variation is performed can become even more relevant than the value of the turbulent Prandtl number itself.

Furthermore, from figure 4(a) it can be seen that for all setups a decrease in turbulent Schmidt number corresponds to an increase in chamber pressure. Regarding the turbulent Prandtl number the trend is not that distinct (cf. figure 4(b)). For most of the cases an increase in turbulent Prandtl number leads to an increase in chamber pressure. However, this is not the case for the k- ω -sst results of IVLR as well as the JAXA computations. At turbulent Schmidt numbers of 0.9 and 1.1 (only 0.9 for JAXA-k- ϵ), increasing the turbulent Prandtl number from 0.7 to 0.9 leads to a rise of chamber pressure. However, a further increase of turbulent Prandtl number from 0.9 to 1.1 results in a pressure decrease (cf. figure 4(b)). This will be discussed further in section B.

Besides the pressure level, the shape of the wall pressure distribution is of interest. It is obtained by normalizing the pressure curve. To establish better comparability to the experimental data, the location of the last pressure sensor, $x = 272.5$ mm, is used as reference position. The corresponding curves are shown in figure 5. The general shape of the wall pressure distribution is similar for all cases. After a short initial section of decay, the pressure quickly rises to its maximum value and keeps declining thereafter. In the front region of the chamber, the profiles show to be right curved. In the rear part, however, curvature depends on the setup as well as on the turbulent Schmidt number. Particularly the k- ϵ results (figures 5(a) and 5(c)) show a flattening of the pressure distribution in the rear section of the chamber. This is clearly visible especially at low turbulent Schmidt numbers. Furthermore, a decrease in turbulent Schmidt number leads to an increase of the pressure drop from the maximum value towards the chamber end, while the initial pressure rise is only weakly affected. This will be addressed further in section B1.

As already observed for the pressure level (cf. figure 4(b)), for most of the cases the influence of the turbulent Prandtl number on the pressure shape can be considered to be minor compared to that of the turbulent Schmidt number. A different behavior is found only for the k- ω -sst results of IVLR and LFA (figures 5(f) and 5(b)) at $Sc_t = 1.1$. There a significant effect of the turbulent Prandtl number is present, which is comparable to that of the turbulent Schmidt number.

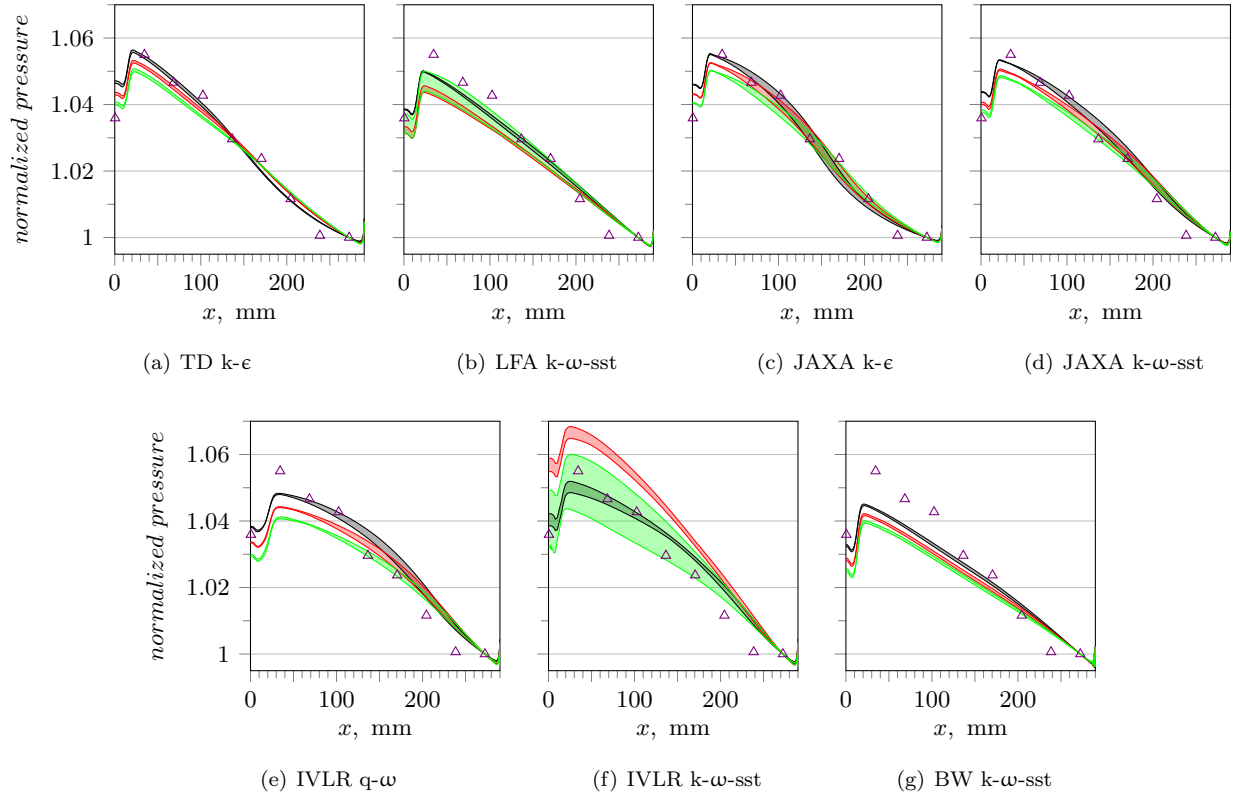


Figure 5. Normalized wall pressure; the colored area corresponds to the range spanned by the different turbulent Prandtl numbers; — $Sc_t = 0.7$, — $Sc_t = 0.9$, — $Sc_t = 1.1$, \triangle experimental data

Regarding the reference data from the experiment, all simulations tend to underpredict the initial relative pressure rise. For $Sc_t = 0.7$ the pressure drop across the chamber is met reasonably well by the k- ϵ and the JAXA-sst results. For the IVLR-sst results the agreement with the experiment highly depends on the turbulent Prandtl number as well. Regarding the curvature of the normalized pressure, the experimental data show a pressure plateau in the rear part of the chamber. This is not precisely reproduced by the simulations whereas the k- ϵ results show the most similar tendency with the pressure distribution flattening out at the chamber exit.

The second validation quantity is the wall heat flux. It has to be kept in mind that the wall heat flux is not only related to the temperature field but depends on species property modeling as well. Figure 6 shows the computational curves. The areas correspond to the range spanned by the results from the different turbulent Schmidt numbers. The overall shape of the wall heat flux is similar for all cases. Starting from the faceplate an initial sharp increase occurs, followed by a short plateau or a slight decrease. Further downstream, a region of increasing wall heat flux at decreasing slope develops. An exception is observed for the Fluent calculations, i.e. the LFA and the TD results. Downstream of $x \approx 200$ mm both show a dependence of the heat flux shape on the turbulent Schmidt number. For low turbulent Schmidt numbers the heat flux tends to a constant value. For high values of the turbulent Schmidt number however, an additional increase occurs in the rear part of the chamber before the curve starts to flatten again. This behavior appears to be solver specific rather than intrinsically related to the turbulence or combustion model.

Regarding the height of the wall heat flux, the finite rate results tend to lie above those of the flamelet based approaches. For the majority of simulations, a decrease in turbulent Schmidt number leads to an increase in heat flux. The reasons for this effect of the turbulent Schmidt number will be discussed in the next section. Across all setups, a decrease of the turbulent Prandtl number results in a higher wall heat

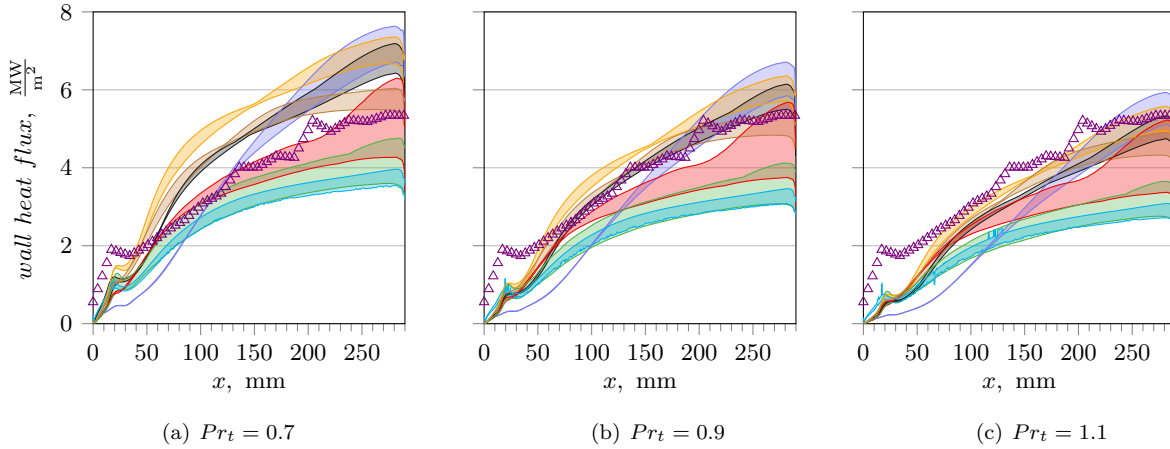


Figure 6. Wall heat flux; the colored area corresponds to the range spanned by the different turbulent Prandtl numbers; — TD $k-\epsilon$, — LFA $k-\omega$ -sst, — JAXA $k-\epsilon$; — JAXA $k-\omega$ -sst, — IVLR $q-\omega$, — IVLR $k-\omega$ -sst, — BW $k-\omega$ -sst, Δ experimental data

flux as well. One factor responsible for this behavior is a higher turbulent transport of energy from the combustion zone to the wall at lower turbulent Prandtl numbers.

A comparison to the experimental data shows that the heat flux in the front part of the chamber is underpredicted by all simulations. It applies: the lower the turbulent Prandtl number, the faster the increase of heat flux close to the faceplate occurs and the better the match between experiment and simulation in this region. Considering the overall shape, the experimental wall heat flux is less smooth than predicted.

B. Mean Flow Characteristics

Advancing from the discussion of the validation quantities in the previous section, now several mean flow parameters are considered. Initially, the global energy balance across the chamber is evaluated, followed by an examination of the underlying axial processes of heat release and mixing. Finally, the role of turbulence for the enthalpy distribution in the chamber is studied.

1. Energy Balance

First, the global pressure level is considered, which is determined by the energy balance across the chamber. This comprises the heat released by combustion as well as the heat losses at the walls. The total amount of chemical power released inside the chamber can be obtained as the value of $\Delta\dot{Q}$ at the chamber exit (cf. figures 7(a) and 7(d)), while the total heat loss is computed via integration of the local heat flux over the chamber surface (cf. figures 7(b) and 7(e)). The difference of these quantities gives the net heat input into the flow, shown in figures 7(c) and 7(f). The distribution of the values for the different cases corresponds reasonably well to the pressure levels shown in figure 3. The trends observed for the relative pressure change in the previous section (cf. figure 4(b)) are found in the energy balance as well. The influence of turbulent Prandtl number is particularly visible for the Prandtl normalized values, given in figures 7(g) to 7(i). For the IVLR-sst results as well as those of JAXA an increase of the turbulent Prandtl number at high turbulent Schmidt numbers leads to a higher net heat release first and a drop thereafter (cf. figure 7(f)). This behavior can be examined further by considering the different quantities going into the net heat release.

For all cases, the heat loss decreases with increasing turbulent Schmidt and Prandtl number (cf. figures 7(b) and 7(e)/7(h)). The same effect of the turbulent Schmidt number can be observed for the heat released (cf. figure 7(a)). The influence of the turbulent Prandtl number however, is not that uniform (cf. figures 7(d)/7(g)). Furthermore, its relevance depends on the combustion model used. The mixture fraction based

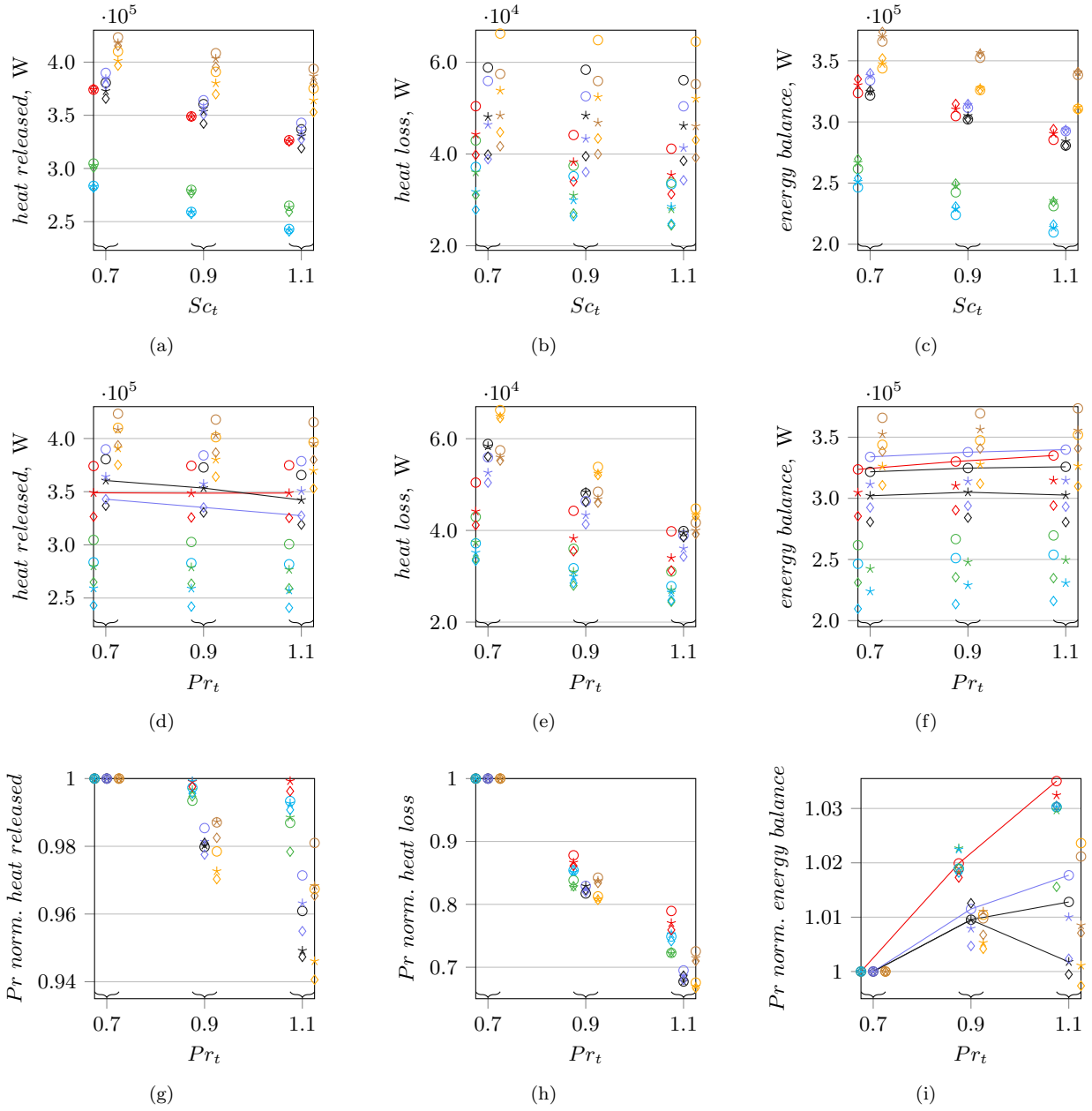


Figure 7. Energy balance; lines included for the visualization of tendencies; — TD k- ϵ , — LFA k- ω -sst, — JAXA k- ϵ , — JAXA k- ω -sst, — IVLR q- ω , — IVLR k- ω -sst, — BW k- ω -sst; $\circ Pr_t / Sc_t = 0.7$, $\ast Pr_t / Sc_t = 0.9$, $\diamond Pr_t / Sc_t = 1.1$

approaches (BW, LFA, TD) show only a smaller dependence on the turbulent Prandtl number compared to the finite rate results. This can be associated with the semi-diabatic setups that retrieve species composition and thus heat release from adiabatic calculations (cf. section III). Correspondingly, the local temperature or enthalpy distribution is of minor importance. In contrast, for the finite rate approaches there is a stronger dependence of the heat released on the turbulent Prandtl number. Its increase results in a lower heat release in the chamber. Several factors are potentially responsible for this tendency. The influence of enthalpy on the combustion process for the finite rate approach might contribute, with the enthalpy released by combustion staying more localized at higher turbulent Prandtl numbers. Furthermore, indirect effects could be involved. For example, small influences of the turbulent Prandtl number on the mixedness at the chamber exit are found for several setups as well (cf. section 2).

The opposite tendencies of heat loss and gain are the reason for the observed behavior of the IVLR-sst and JAXA results. The energy balance (cf. figure 7(f)) shows that while the reduction of heat loss exceeds the reduction of heat release in most of the cases, at turbulent Schmidt numbers of 0.9 and 1.1 the net energy in the system reduces for the setups under consideration.

Furthermore, the increase of heat release with decreasing turbulent Schmidt number explains the tendency of an increasing relative pressure loss across the chamber found in section A. By analogy with a Rayleigh flow, an increase of heat release tends to cause a higher pressure loss. Moreover, the influence of turbulent Prandtl or Schmidt number on the the heat release might contribute to their effect on the wall heat flux observed in the previous section.

2. Heat Release and Mixing

While the global energy balance is suitable for the explanation of the overall tendencies, it does not provide any information about the local flow behavior. Consequently, the focus is turned now from the quantitative analysis to qualitative aspects of the axially resolved heat released, $\Delta\dot{Q}$. The link between pressure and heat release discussed above persists locally as well: especially in the rear part of the chamber the heat release rate, i.e. the axial gradient of heat released, and the axial gradient of wall pressure possess comparable shapes. This is consistent with the considerations regarding the Rayleigh flow in the previous section. For further discussing the shape of the heat released in the cylindrical part of the combustion chamber is considered. There the difference of the heat released to a linear development, corresponding to a constant heat release rate at equal total magnitude, is calculated. The result is normalized by the maximum value of heat released, located at the sections' end. This gives:

$$\Delta\dot{Q}_s = \frac{1}{\max(\Delta\dot{Q})} \cdot \left(\Delta\dot{Q} - \max(\Delta\dot{Q}) \cdot \frac{x}{290 \text{ mm}} \right) \quad . \quad (12)$$

A positive value of $\Delta\dot{Q}_s$ indicates that at the respective position x more heat has been released than it would be the case for an axially uniform distributed heat source. An increase of $\Delta\dot{Q}_s$ means that more heat is released at the current position than for a uniform heat source distribution and vice versa for a decreasing $\Delta\dot{Q}_s$. Thus the profiles of $\Delta\dot{Q}_s$, shown in figure 8, do not correspond to the absolute values of heat released. One curve exceeding the other just means that a higher portion of the total heat release has already occurred.

Considering the axial development of heat released (figure 8), the approaches differ in behavior. Two influencing factors are clearly visible: the turbulence model on the one hand and the combustion modeling approach on the other hand. The latter is particularly related to the sensitivity to the turbulent Prandtl number.

Most of the k- ω -sst cases show a maximum located in the front half of the chamber, particularly at high values of the turbulent Schmidt number. Correspondingly, heat release is higher than average in the front part and stays lower thereafter. In contrast, the k- ϵ results (cf. figures 8(a) and 8(c)) possess a more even distribution of the heat release, indicating a higher contribution of the rear part of the chamber to the overall heat release. There a second region of high heat release forms, denoted by a slower decrease or even increase of $\Delta\dot{Q}_s$. For low turbulent Schmidt numbers the location of maximum $\Delta\dot{Q}_s$ can actually shift to the rear

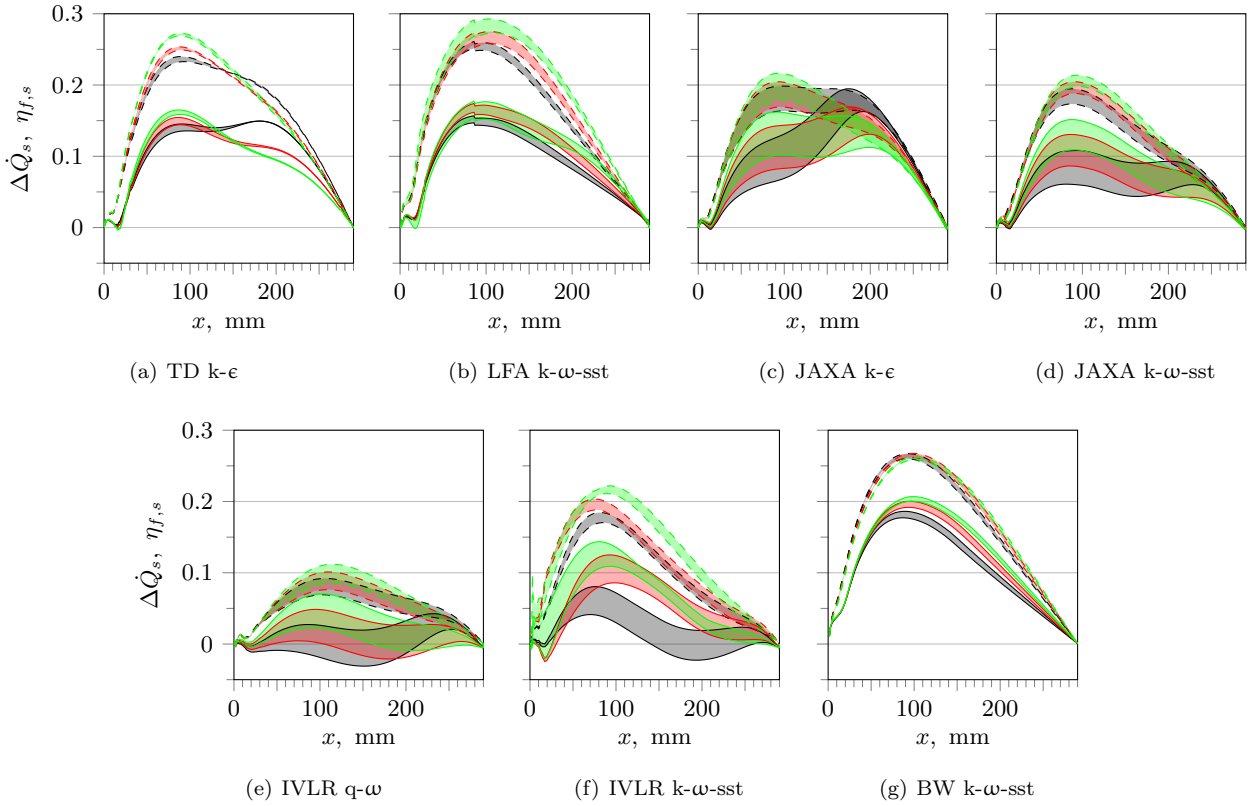


Figure 8. Normalized heat released and normalized mixedness; the colored area corresponds to the range spanned by the different turbulent Prandtl numbers; — $Sc_t = 0.7$, — $Sc_t = 0.9$, — $Sc_t = 1.1$; — normalized heat released, - - - normalized mixing

section of the chamber. The $q-\omega$ computations are closest to a constant heat release. Again, the rear part of the chamber plays a more important role at low turbulent Schmidt numbers.

In the finite rate simulations the heat released is notably influenced by the turbulent Prandtl number. As the turbulent Prandtl number decreases, the heat release shifts towards the front part of the chamber. The flamelet results, however, show a much weaker influence of the turbulent Prandtl number. Furthermore, for the finite rate approaches the relevance of the rear chamber section tends to be higher than for the flamelet results.

The heat released is closely linked to the mixing process in the chamber, which is assumed to be turbulence dominated. Analogous to $\Delta\dot{Q}_s$ for the heat released, the variable $\eta_{f,s}$ is defined based on η_f (cf. section IV B). This allows to study the qualitative development of mixedness. The corresponding curves are given in figure 8. It has to be kept in mind that the mixedness parameter is defined as a standard deviation and thus there is no explicit physical relation to the heat released. Nevertheless, the development of mixedness and heat released are similar to each other for all cases. Considering the finite rate results, the smaller y-wise extension of the colored areas (cf. figure 8) for the mixedness evolution compared to $\Delta\dot{Q}_s$ indicates a weaker influence of the turbulent Prandtl number on mixing than on heat release. At the same time no significant effect of the turbulent Prandtl number on mixing is found for the flamelet approaches, corresponding to the observations made for the heat release. This supports the conclusion that the sensitivity of heat release, and thus pressure, to the turbulent Prandtl number is linked to chemical kinetics being influenced by the enthalpy distribution.

For quantitative comparison, the mixedness at the chamber exit is shown in figure 9. With decreasing turbulent Schmidt number, mixedness increases notably, while the effect of turbulent Prandtl number is

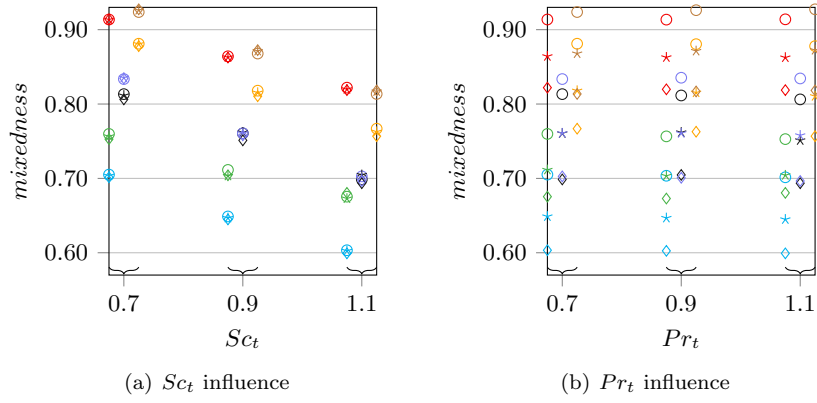


Figure 9. Mixedness at chamber exit; — TD k- ϵ , — LFA k- ω -sst, — JAXA k- ϵ , — JAXA k- ω -sst, — IVLR q- ω , — IVLR k- ω -sst, — BW k- ω -sst; \circ $Pr_t / Sc_t = 0.7$, $*$ $Pr_t / Sc_t = 0.9$, \diamond $Pr_t / Sc_t = 1.1$

far smaller, staying below 1 %. The k- ϵ results predict the most complete mixing. The weakest mixing is observed for the flamelet-sst results. Comparing the mixedness to the heat released (figures 7(b) and 7(e)) the coupling between heat release and mixing progress is visible.

3. Enthalpy Stratification

The third parameter employed to describe the internal flow is the enthalpy stratification η_h . The axial development of this quantity is plotted in figure 10. For all cases the stratification decrease is fast in the front part of the chamber, slowing down further downstream. It stands out that the finite rate approaches show that the turbulent Prandtl number is of more importance than the turbulent Schmidt number, while the opposite is the case for the mixture fraction based approaches. This will be addressed further below. There are influences of combustion as well as turbulence model. Most of the results, particularly the k- ϵ based ones, show a decrease of the slope of the stratification parameter curve in the rear part of the chamber. The faster the homogenization, the earlier the flattening occurs. In contrast, the flamelet-sst results show a continuing decrease of enthalpy stratification at the chamber exit. Furthermore, they predict a higher enthalpy stratification compared to the other setups. The tendency of slower homogenization for the k- ω -sst simulations than for the k- ϵ results is observed in the JAXA computations as well. The IVLR predictions stay quite similar to each other through the whole chamber. Across the different combustion modeling approaches, the k- ϵ results of JAXA and TD show comparable predictions.

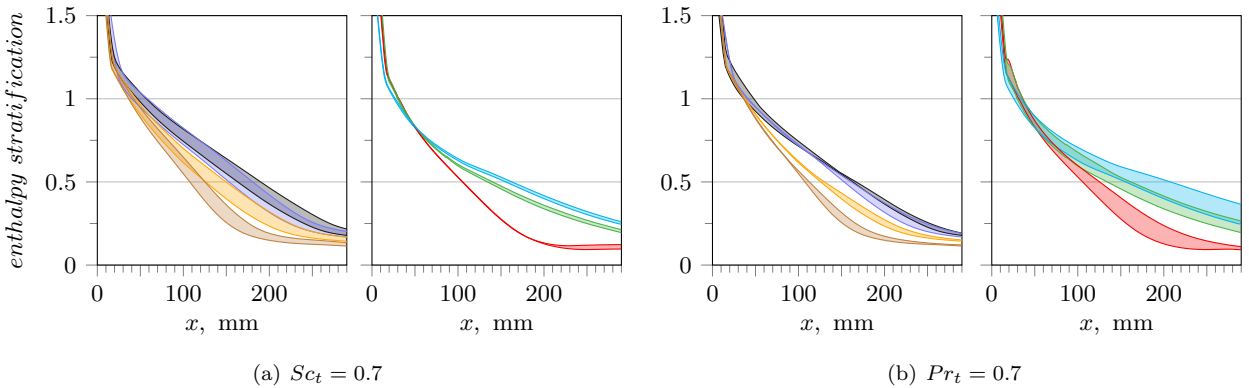


Figure 10. Enthalpy stratification; the colored area corresponds to the range spanned by the different turbulent Prandtl or Schmidt numbers respectively; — TD k- ϵ , — LFA k- ω -sst, — JAXA k- ϵ , — JAXA k- ω -sst, — IVLR q- ω , — IVLR k- ω -sst, — BW k- ω -sst

The species mixing, discussed using η_f in the previous section, is mainly related to the diffusion terms in the mixture fraction or species transport equations. In contrast, several influencing factors go into the enthalpy stratification parameter. On the one hand, there is the distribution of absolute enthalpy^b. The turbulence influence on this quantity is modeled via the term given in Eq. (2). On the other hand, the actual profile of the sensible enthalpy is a result of the reactions as well since they determine which portion of absolute enthalpy is converted into sensible enthalpy. The fact that the turbulent Schmidt number does not enter into the energy equation indicates that the observed sensitivity of η_h to this parameter results from indirect effects. To look into this, radial profiles of the sensible enthalpy, the heat of formation and the absolute enthalpy are studied. Figure 11 shows the corresponding curves close to the chamber exit at $x = 250$ mm.

For absolute enthalpy (figure 11(a)) there is a considerable difference between the results obtained with finite rate chemistry and those computed with mixture fraction based approaches. The finite rate results show a significant influence of both, turbulent Prandtl and Schmidt number on the shape of the absolute enthalpy. For the flamelet approaches the effect is much weaker and hardly affects the qualitative distribution. However, the absolute enthalpy can be regarded as a superposition of sensible enthalpy and heat of formation. Across all cases the generic shape of each of these two quantities (figures 11(b) and 11(c)) is similar, independent of the turbulent Prandtl or Schmidt number.

While the generic shape of sensible enthalpy and heat of formation respectively remains unchanged, notable differences occur regarding the quantitative distribution across the cases. First, there is a dependence on the turbulence model. In the k- ϵ results (TD and JAXA k- ϵ) a lower radial stratification occurs. In contrast, the ω based results show a more pronounced peak for the sensible enthalpy or trough for the heat of formation. This corresponds to the k- ϵ simulations predicting a higher degree of mixedness at the chamber exit. In addition, the dependence of the stratification of sensible enthalpy on the turbulence model is not fully reflected in the distribution of absolute enthalpy (cf. TD/LFA and JAXA k- ϵ /k- ω -sst in figure 11). These observations indicate the influence of indirect effects as stated above. A comparable behavior is found for the dependence on the turbulent Schmidt number for the TD computations. The absolute enthalpy (cf. figure 11(a)) shows only a negligible influence of the turbulent Schmidt number. However, the stratification parameter (figure 10) is sensitive to the turbulent Schmidt number as is the sensible enthalpy (cf. figure 11(b)). This indicates that the redistribution of the mixture fraction and thus the flow composition rather than the turbulent transport of the sensible enthalpy are responsible for the influence of the turbulent Schmidt number. This behavior can be confirmed for the IVLR results as well. They show very similar absolute enthalpy profiles for the different turbulence models but differ notably in sensible enthalpy. Accordingly, the influence of the turbulence model on the enthalpy stratification manifests itself via the reactions more than via the distribution of absolute enthalpy.

Furthermore, the qualitative influence of turbulent Prandtl and Schmidt number on enthalpy stratification differs between the combustion models. For the flamelet results, the sensitivity of absolute and sensible enthalpy towards the turbulent Prandtl number, if present, is found to be rather uniform across the chamber radius. In contrast, the turbulent Schmidt number significantly influences the radial stratification. For most of the finite rate results the influence of the turbulent Prandtl number tends to be less uniformly distributed. This possibly contributes to the difference between the combustion models that has been observed regarding the sensitivity of the enthalpy stratification parameter to the turbulent Prandtl and Schmidt numbers.

The wall heat flux is closely linked to the enthalpy field. However, its behavior is not captured by the enthalpy stratification parameter (cf. figure 10). Indeed other parameters, particularly heat release, can significantly influence the wall heat flux as well. However, for the flamelet results neither of both quantities shows a dependence on the turbulent Prandtl number comparable to that observed for the wall heat flux. The radial distribution of sensible enthalpy (cf. figure 11(b)) shows that the influence of turbulent Prandtl and Schmidt number is present over a considerable range across the radius. The wall heat flux however, is determined by the temperature profile close to the wall. This limited radial section of the chamber does not dominate the enthalpy stratification parameter. Therefore, the notable influence of turbulent Prandtl number on heat flux is not considerably correlated with this quantity.

^bThis term is used here to refer to the sum of sensible enthalpy and heat of formation. The kinetic energy part can be neglected for this discussion.

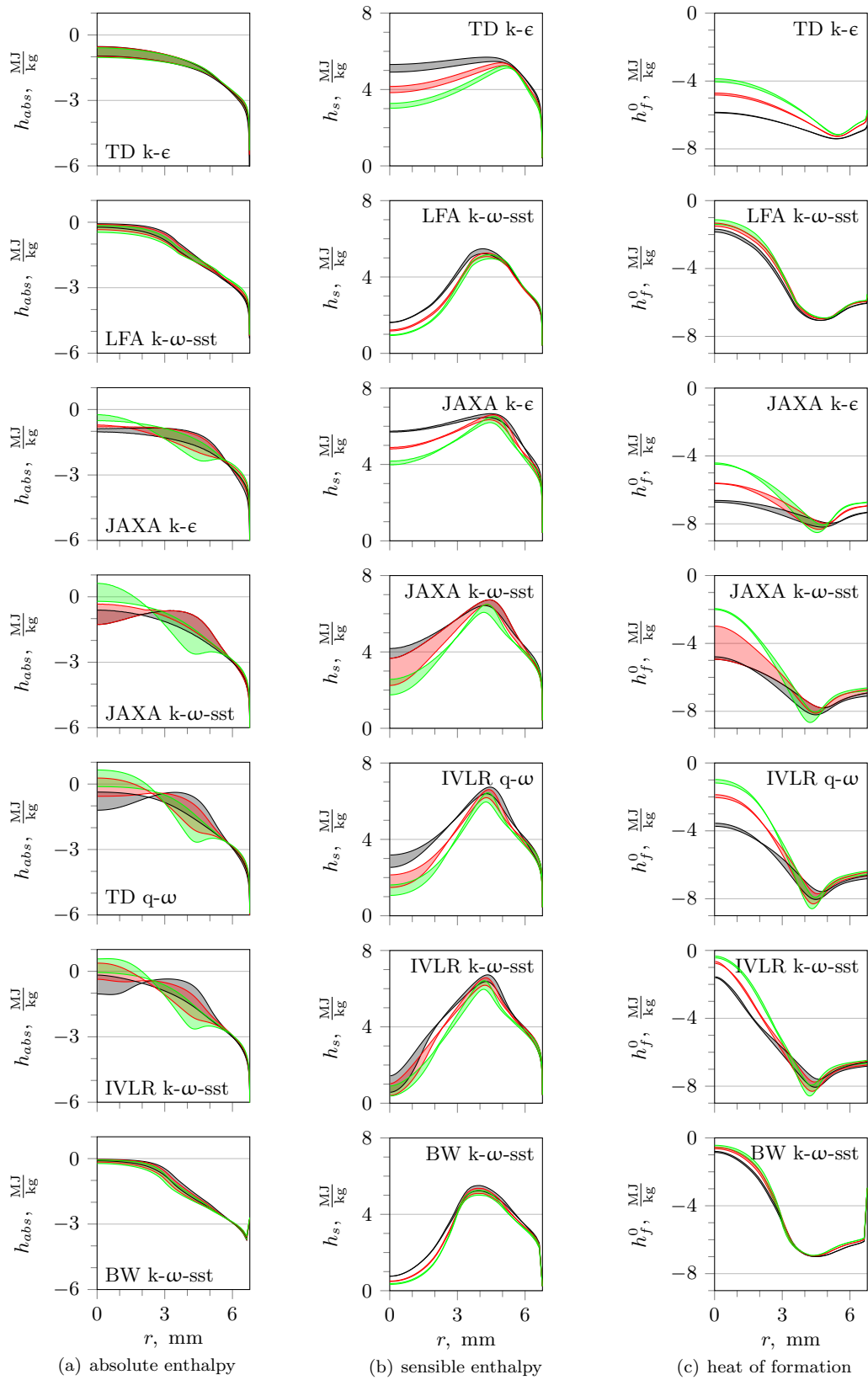


Figure 11. Radial profiles at $x = 250$ mm; the colored area corresponds to the range spanned by the different turbulent Prandtl numbers; — $Sc_t = 0.7$, — $Sc_t = 0.9$, — $Sc_t = 1.1$

C. Turbulence-Mean-Flow-Coupling and Turbulence Quantities

In the previous section the process of species and enthalpy mixing as well as the heat released have been studied. The connection between heat released and mixing has been shown. Now, in a third step the underlying fields of turbulent viscosity, the quantity representing the effect of turbulence in the conservation and transport equations, will be looked upon. Figure 12 (left) shows contour plots of the turbulent viscosity for the different setups at $Sc_t = Pr_t = 0.7$. While there is an influence of the values of turbulent Prandtl and Schmidt numbers on the quantitative distribution in this field, the characteristic structure of each setup remains unchanged. Thus, only this single configuration is discussed further.

All cases show a core of high turbulent viscosity emanating from the oxygen inlet channel at the axis, which attenuates further downstream. In the outer flow region close to the face plate a spot of high turbulent viscosity is located, corresponding to the recirculation zone. Here the highest turbulent viscosity occurs. Further downstream, the behavior depends on the turbulence model. The k- ϵ based results (figures 12(a) and 12(c)) as well as the q- ω case (figure 12(e)) show a second region of high turbulent viscosity in the rear part of the chamber. In comparison to results computed with the same code but with different turbulence models, for the k- ω -sst results this second region is much weaker or even not existent. This characteristic behavior is consistent with the observations from section B. There, it has been stated that for the k- ϵ results there is a higher contribution of the rear part of the chamber to heat release and mixing than for the k- ω -sst results. Across the combustion models, the finite rate based results show a more intense secondary region than the flamelet based ones.

In the region close to the oxygen injector the turbulent viscosity notably differs between results computed with the same basic setup but different turbulence models. However, this is not reflected in the overall mixing behavior (cf. figure 8). This indicates that the effect of an increased turbulent viscosity in this region is restricted to the oxidizer core and thus does not improve the average mixedness.

Finally, the turbulent quantities are considered (cf. figures 12 middle and right). For better comparability the turbulent kinetic energy is visualized for the q- ω -model instead of q and the corresponding ω field is scaled to compensate for different definitions compared to the k- ω -sst models (cf. section A).

Some structures observed for the turbulent viscosity are visible for the turbulence quantities as well. Particularly for the k- ϵ based results, a wide region of high turbulent kinetic energy is found in the rear part. However, the exact contours differ from those of the turbulent viscosity. Furthermore, the fields of the corresponding dissipation quantity show comparable structures. For the k- ω -sst results characteristic structures of the turbulence model are visible as well, particularly when comparing results computed with the same combustion model. Again, these structures do not clearly match the field of turbulent viscosity. Altogether, no distinct tendencies are visible that allow the reduction of the observed differences in turbulent viscosity to turbulent kinetic energy or dissipation alone. In contrast, the different effects of turbulence result from the combination of both quantities.

VI. Conclusion

The flow inside a single element GOX/GCH₄ combustion chamber has been simulated. Results obtained by five different groups with various codes, combustion and turbulence models have been compared with each other. Validation data from the corresponding experiment have been considered and the underlying effects have been traced down to the level of turbulence modeling. Furthermore, the effects of turbulent Prandtl and Schmidt numbers have been studied.

A relation between pressure, heat release and mixing inside the chamber has been found. The characteristic behavior of these quantities depends on the specific turbulence model used in the computations. For simulations using the k- ϵ model a higher contribution of the rear part of the chamber to heat release

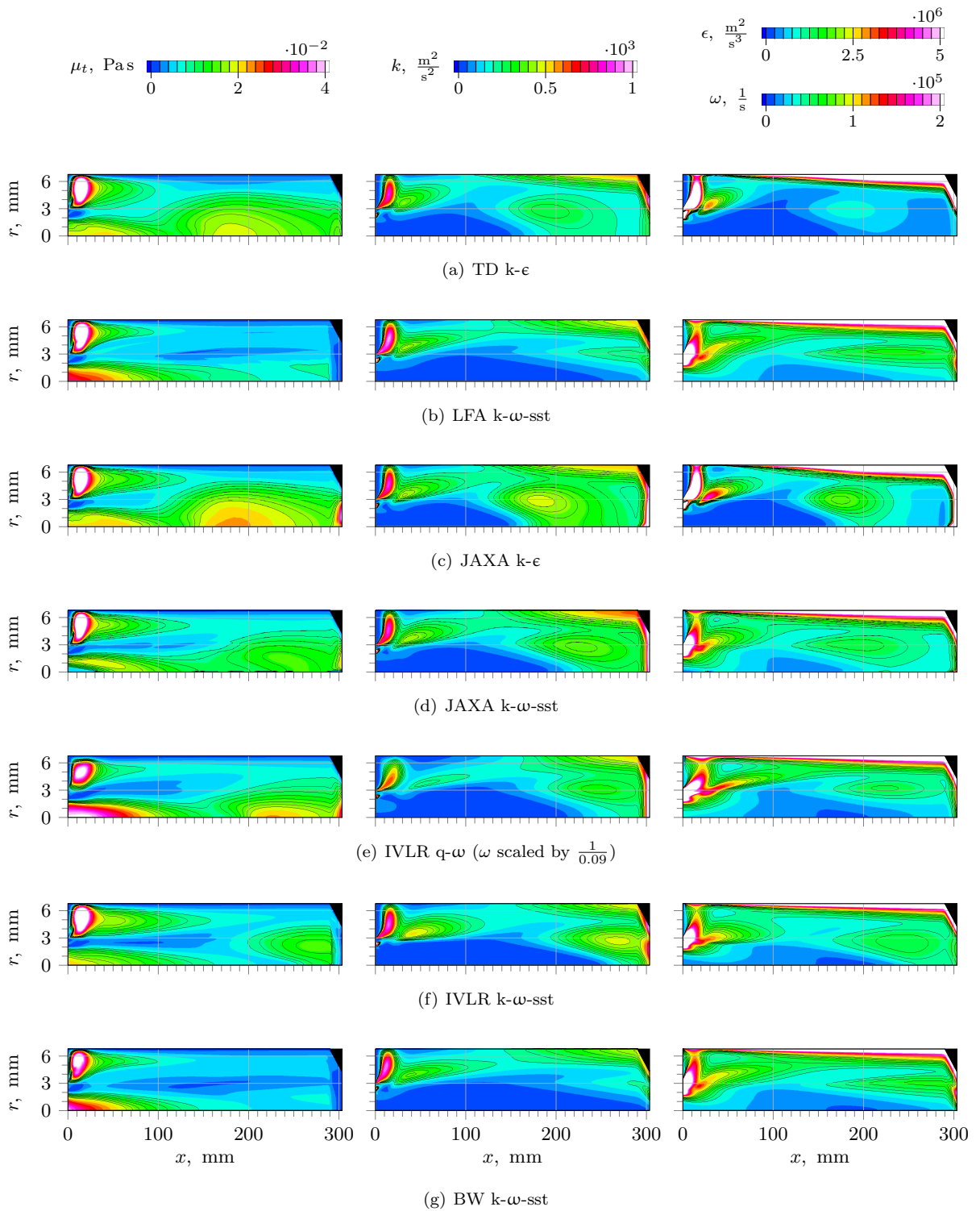


Figure 12. Contour plots of turbulent viscosity (left), turbulent kinetic energy (middle) and turbulent dissipation (right); radial direction scaled by a factor of 10

and mixing is observed compared to $k-\omega$ -sst based results. Furthermore $k-\omega$ -sst simulations show a weaker overall mixing and heat release, resulting in a lower chamber pressure. These tendencies have been found to originate from the fields of turbulent viscosity. Regions of high turbulent viscosity exist in the rear section of the chamber for $k-\epsilon$ models. For $k-\omega$ -sst approaches these zones are weaker or even non existent.

All results are sensitive to the turbulent Schmidt numbers. The importance of the turbulent Prandtl number, however, has been found to be higher for setups based on finite rate chemistry than for the semi-diabatic flamelet approaches. This applies to chamber pressure, mixing, heat release and enthalpy stratification. The higher dependence of the finite rate results on the turbulent Prandtl number has been related to the influence of local enthalpy on reaction. The sensitivity of the enthalpy stratification to the turbulent Prandtl and Schmidt number respectively has been found out to be a result of combustion effects rather than the redistribution of the absolute enthalpy. As a consequence, for the mixture fraction based approaches the enthalpy stratification predominantly depends on the turbulent Schmidt number.

For future work, the effects leading to the differences observed in the turbulent viscosity should be identified. This requires a detailed examination of the turbulence models' implementations in the employed codes. Moreover, the relevance of turbulence modeling should be studied further by performing simulations using the same field of turbulent viscosity.

VII. Acknowledgments

Financial support has been provided by the German Research Foundation (Deutsche Forschungsgemeinschaft - DFG) in the framework of the Sonderforschungsbereich Transregio 40.

References

- ¹Roth, C. M. et al., "Comparison of different modeling approaches for CFD simulations of a single-element GCH₄/GOX rocket combustor," *Sonderforschungsbereich/Transregio 40 – Summer Program Report 2015*, 2015.
- ²Roth, C. M. et al., "Numerical Investigation of Flow and Combustion in a Single-Element GCH₄/GOX Rocket Combustor," submitted to 52nd AIAA/SAE/ASEE Joint Propulsion Conference.
- ³Maestro, D. et al., "Numerical Investigation of Flow and Combustion in a Single-Element GCH₄/GOX Rocket Combustor: Chemistry Modeling and Turbulence-Combustion Interaction," submitted to 52nd AIAA/SAE/ASEE Joint Propulsion Conference.
- ⁴Haidn, O., Knab, O., Celano, M., Kirchberger, C., and Schlieben, G., "Transregio SFB-TR40 – Test Case 1," Tech. Rep. 6, Technische Universität München, Lehrstuhl für Flugantriebe, 2015.
- ⁵Slavinskaya, N., Abbasi, A., Weinschenk, M., and Haidn, O., "Methane Skeletal Mechanism for Space Propulsion Applications," *5th International Workshop on Model Reduction in Reacting Flows*, 2015.
- ⁶Smith, G. et al., "GRI-Mech 3.0, The Gas Research Institute," http://www.me.berkeley.edu/gri_mech/.
- ⁷*Fluent Theory Guide*, Product Documentation ANSYS Inc. Release 16.0.
- ⁸Launder, B. and Spalding, D. B., *Lectures in Mathematical Models of Turbulence*, London: Academic Press, 1972.
- ⁹*Fluent Theory Guide*, Product Documentation ANSYS Inc. Release 15.0.
- ¹⁰Menter, F. R., "Two-Equation Eddy-Viscosity Turbulence Models for Engineering Applications," *AIAA Journal*, Vol. 32, 1994.
- ¹¹Coakley, T. and Huang, P., "Turbulence modeling for high speed flows," *Aerospace Sciences Meetings*, American Institute of Aeronautics and Astronautics, Jan. 1992.
- ¹²Müller, H., Niedermeier, C. A., Matheis, J., Pfitzner, M., and Hickel, S., "Large-eddy simulation of nitrogen injection at trans- and supercritical conditions," *Physics of Fluids (1994-present)*, Vol. 28, No. 1, 2016, pp. 015102.
- ¹³Müller, H., Matheis, J., Pfitzner, M., and Hickel, S., "Large-Eddy Simulation of coaxial LN₂/GH₂ injection at trans- and supercritical conditions," *Journal of Propulsion and Power*, Vol. 32, No. 1, 2016, pp. 46–56.
- ¹⁴Müller, H. and Pfitzner, M., "Large-Eddy Simulation of transcritical LO_x/CH₄ jet flames," *6th European Conference for Aeronautics and Space Sciences (EUCASS)*, Krakau, 2015.